



Title	Analyzing multistep homogeneous nucleation in vapor-to-solid transitions using molecular dynamics simulations
Author(s)	Tanaka, Kyoko K; Diemand, Jürg; Tanaka, Hidekazu; Angéilil, Raymond
Citation	Physical Review E, 96, 022804 https://doi.org/10.1103/PhysRevE.96.022804
Issue Date	2017-08-28
Doc URL	http://hdl.handle.net/2115/67056
Rights	©2017 American Physical Society
Type	article
File Information	PhysRevE.96.022804.pdf



[Instructions for use](#)

Analyzing multistep homogeneous nucleation in vapor-to-solid transitions using molecular dynamics simulations

Kyoko K. Tanaka,^{1,*} Jürg Diemand,² Hidekazu Tanaka,³ and Raymond Angéllil²

¹*Institute of Low Temperature Science, Hokkaido University, Sapporo 060-0819, Japan*

²*Institute for Computational Science, University of Zürich, 8057 Zürich, Switzerland*

³*Astronomical Institute, Graduate School of Science, Tohoku University, Sendai 980-8578, Japan*

(Received 20 April 2017; published 28 August 2017)

In this paper, we present multistep homogeneous nucleations in vapor-to-solid transitions as revealed by molecular dynamics simulations on Lennard-Jones molecules, where liquidlike clusters are created and crystallized. During a long, direct NVE (constant volume, energy, and number of molecules) involving the integration of $(1.9\text{--}15) \times 10^6$ molecules in up to 200 million steps ($=4.3 \mu\text{s}$), crystallization in many large, supercooled nanoclusters is observed once the liquid clusters grow to a certain size (~ 800 molecules for the case of $T \simeq 0.5\varepsilon/k$). In the simulations, we discovered an interesting process associated with crystallization: the solid clusters lost 2–5 % of their mass during crystallization at low temperatures below their melting temperatures. Although the crystallized clusters were heated by latent heat, they were stabilized by cooling due to evaporation. The clusters crystallized quickly and completely except at surface layers. However, they did not have stable crystal structures, rather they had metastable structures such as icosahedral, decahedral, face-centered-cubic-rich (fcc-rich), and hexagonal-close-packed-rich (hcp-rich). Several kinds of cluster structures coexisted in the same size range of $\sim 1000\text{--}5000$ molecules. Our results imply that multistep nucleation is a common first stage of condensation from vapor to solid.

DOI: [10.1103/PhysRevE.96.022804](https://doi.org/10.1103/PhysRevE.96.022804)

I. INTRODUCTION

Crystallization from vapor is a phase transition that plays an important role in many areas of science and technology. The phase transitions start through nucleation, where unstable equilibrium clusters of a new phase called critical nuclei form first and then grow continuously. Although crystallization is expected below the triple point temperature, it has often been observed, in nature and experiments, that nuclei formed from vapor are supercooled liquid droplets [1–5]. This is an example of Ostwald’s step rule [1], where a metastable phase appears first before a stable phase. Even though the transition from vapor to solid is a familiar process, it is not yet fully understood even for simple homogeneous nucleation. One reason for this is that unstable nanosized nuclei are difficult to observe. The structure of nanocrystal clusters is also important in scientific and technological applications [6–9]. It is known that the structure of an atomic cluster is a function of material component and temperature as well as the number of atoms in the cluster [9–21]. Many theoretical calculations and experiments have been conducted on size-dependent structures in atomic clusters for various materials, and they have shown that structures for nanoclusters have a variety of characteristics [9,11,15,18–20,22].

Molecular dynamics (MD) simulations can directly resolve details of the nucleation process and provide useful information. Although many studies have focused on vapor-to-liquid nucleation by MD simulations [23–29], few have considered vapor-to-solid nucleation [30,31]. A multistep nucleation for the vapor-to-solid transition was observed in [30], but no detailed analysis of the crystallization process was conducted.

For nucleation from vapor, past studies have typically simulated up to 10^5 molecules. Large-scale direct (NVE and NVT) MD simulations with up to $\sim 10^9$ molecules were recently reported [29,32,33]. Diemand *et al.* [29] were able to resolve significantly lower nucleation rates for the vapor-to-liquid transition than past work, and they obtained the first results of MD nucleation that are directly comparable to those of laboratory experiments [29]. In [29], however, crystallization of the liquid particles was not observed. With a longer period of integration, the large number of liquid supercooled nanoparticles forming naturally out of the vapor allow us to study particle crystallization in detail. This approach can help gather important statistics for the crystallization of particles.

In this study, we report MD simulations of the vapor-to-solid transition to investigate the multistep nucleation process and crystallization in the liquid droplets. Since a relatively long simulation time is needed to observe the crystallization of droplets, we performed long-term MD simulations with $\sim 10^8$ time steps ($\sim \mu\text{s}$) using 2–15 million Lennard-Jones molecules at low temperature. During a long, direct NVE integration in the simulations, the supercooled nanoclusters crystallized naturally during their growth. We highlight an interesting process associated with the crystallization, whereby the solid clusters lost part of their masses at crystallization. We also show that the nanoclusters composed of $\sim 1000\text{--}5000$ molecules exhibit a variety of characteristic structures. The results also allow us to evaluate the nucleation rate in crystallization. We compare the rate thus obtained with a theoretical evaluation to test nucleation theory.

II. SIMULATIONS AND ANALYSIS

The simulations were performed on the LAMMPS (Large-scale Atomic Molecular Massively Parallel Simulator),

*kktanaka@lowtem.hokudai.ac.jp

TABLE I. Simulation properties: temperature T , number of molecules N , periodic cube size L , molecule number density n , total run time t_{end} , and nominal initial supersaturation $S_0 = P_0/P_{\text{sat}}$, where P_{sat} is the saturated vapor pressure, and the pressure P_0 is calculated by assuming that all molecules are in the form of monomers.

Run ID	T (ϵ/k)	N (10^6)	L (σ)	n_0 ($10^{-4}\sigma^{-3}$)	t_{end} ($10^6\tau$)	S_0
T3n18	0.3	1.95	2214	1.8	2.0	21000
T3n20L	0.3	15.6	4272	2.0	1.5	24000
T3n20S	0.3	1.95	2137	2.0	1.5	24000
T3n22	0.3	1.95	2070	2.2	1.5	26000
T3n24	0.3	1.95	2011	2.4	1.4	28000

developed at Sandia National Laboratories [34]. We used the Lennard-Jones (LJ) potential

$$u(r) = 4\epsilon \left[\left(\frac{\sigma}{r} \right)^{12} - \left(\frac{\sigma}{r} \right)^6 \right] \quad (1)$$

with a cutoff at 5σ . In the argon system, the units were $\epsilon/k = 119.8$ K, $\sigma = 3.405$ Å, $m = 6.634 \times 10^{-23}$ g, and $\tau = 2.16$ ps. The simulations box had periodic boundary conditions, and the time steps were set to $\Delta t = 0.01\tau = 0.01\sigma\sqrt{m/\epsilon}$, in the same way as the previous simulations for the vapor-to-liquid nucleation [29,30].

Most previous MD simulations of nucleation from vapor have been performed on NVT (constant number of molecules, volume, and temperature) ensembles, where the temperature was set as constant by a thermostat, such as the Nosé-Hoover method or the rescaling of velocity. However, it is possible that a thermostat used in the MD simulation influences the crystallization of the particles because, through the thermostat, part of the latent heat released at crystallization is removed from the interior and the surface of the clusters [31]. To avoid unnatural heat transfer with the thermostat, we used NVE (constant energy) ensembles in our MD simulations. In the Appendix, we discuss how the thermostat influences the results.

Clusters were defined using the Stillinger criterion with a search radius of 1.52σ [29,30]. The crystal structure was identified using the common neighbor analysis (CNA) method [35,36] implemented in LAMMPS. The cutoff distance to the nearest-neighbor search was set to 1.3σ . Similar results were obtained using 1.4σ , whereas cutoff lengths below or above this range failed to identify crystal structures. The initial temperature was set to $0.3\epsilon/k$ (36 K for argon). Such properties as the initial number density, used to set up the simulations, are given in Table I. The initial supersaturation was 21 000–28 000 at saturated vapor pressure, $P_{\text{sat}} = 2.53 \times 10^{-9}\epsilon\sigma^{-3}$ at $T = 0.3\epsilon/k$.

III. RESULTS

A. Nucleation and crystallization of particles

We first present the results of the MD simulation when using 15 million LJ molecules (T3n20L in Table I). During the long, direct NVE integration (1.6 million $\tau = 3.5\mu\text{s}$), a condensation of 115 large, liquidlike (>800 molecules) supercooled

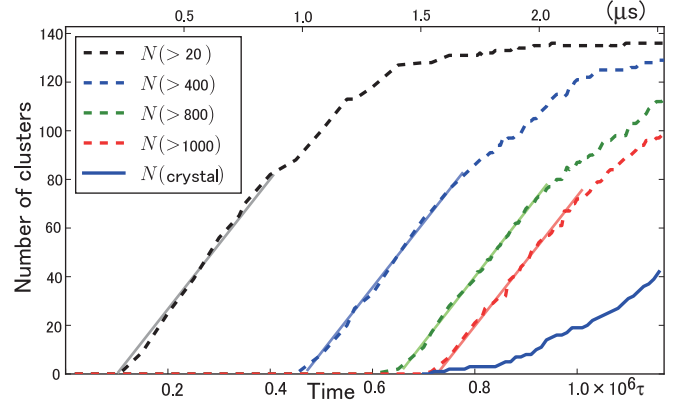


FIG. 1. Time evolution of the number of clusters larger than various thresholds (20, 400, 800, and 1000 molecules) for run T3n20L. The solid line shows the number of crystallized clusters. The vapor-to-liquid nucleation rate was estimated to be $J = 3.2 \times 10^{-15}\sigma^{-3}\tau^{-1}$. The fitted slope is shown along the thin lines.

nanoclusters was observed. Figure 1 shows the time evolution of the number of clusters for run T3n20L. After an initial lag time, homogeneous vapor-to-liquid nucleation started, and the number of stable clusters grew at a constant nucleation rate of $J = 3.2 \times 10^{-15}\sigma^{-3}\tau^{-1}$ ($= 3.2 \times 10^{19} \text{ cm}^{-3} \text{ s}^{-1}$), which was measured from the slopes in Fig. 1. This rate subsequently decreased as the latent heat caused a temperature increase and, therefore, a lower supersaturation of the vapor. As shown in Fig. 1, crystallization started at approximately $7 \times 10^5\tau$ ($= 1.5\mu\text{s}$). At the end of the run, one-third of the large clusters ($N > 800$) were frozen and all five of the largest ones ($N > 2400$) were still liquid. The latent heat from the vapor-to-liquid transition led to liquid cluster temperatures above the vapor temperature. Furthermore, the additional latent heat from the crystallization caused the solid cluster to become hotter than the liquid droplet, as described in Sec. III B.

Figure 2 shows the size distribution of clusters at the end of the simulation ($1.97 \times 10^6\tau$). The smallest frozen cluster contained 898 molecules, but not all clusters froze once they had attained a similar mass: some froze at larger sizes, and others did not freeze at all. We observed that 41 of them crystallized quickly, and almost completely, in the simulation. From the MD simulations, the resulting liquid-to-solid nucleation rate was calculated at approximately $J_c = 8.6 \times 10^{-10}\sigma^{-3}\tau^{-1}$ ($= 1.0 \times 10^{25} \text{ cm}^{-3} \text{ s}^{-1}$) as follows: The 41 crystallization events occurred during $4.6 \times 10^5\tau$ from $7 \times 10^5\tau$ to $1.16 \times 10^6\tau$. There were 1.92×10^5 molecules in clusters of size greater than 800 molecules after $1.16 \times 10^6\tau$. Since the density of the clusters was $\rho = 0.92$, $2.08 \times 10^5\sigma^3$ was the available volume at the end. Since this increased roughly linearly with time, assuming a time-averaged volume of liquid half this value, $J_c = 41/(460\,000\tau \times 104\,000\sigma^3) = 8.6 \times 10^{-10}\tau^{-1}\sigma^{-3}$.

A snapshot taken at the end of run T3n20L is shown in Fig. 3. It shows a 15%-wide slice through the computational box colored by the local number density. A projection and two slices through a large, solid cluster (2313 molecules) in the snapshot are shown in the insets. The colors in the insets

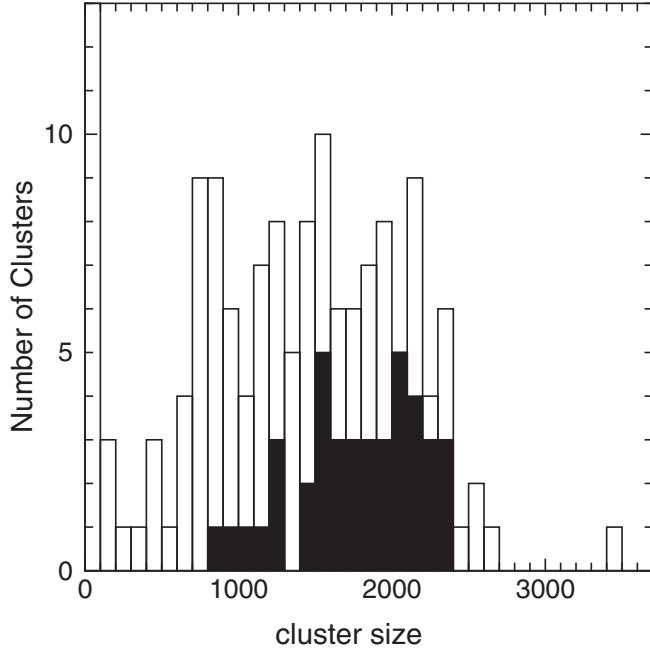


FIG. 2. Size distributions of liquid clusters (white) and crystallized clusters (black) at the end of run T3n20L.

illustrate the crystal structure found by the CNA algorithm: blue is a face-centered-cubic structure (fcc), red is a hexagonal-close-packed structure (hcp), and white is unknown/amorphous. The core contained the fcc and hcp layers. The outer parts had lower densities and were amorphous, but they were still clearly well-ordered with the exception of the outermost atomic layer. Their cores contained predominantly fcc and hcp structures. Clusters with body-centered-cubic (bcc) structures were not found in our MD simulations: they did not play an important role in the crystallization process under the conditions we simulated.

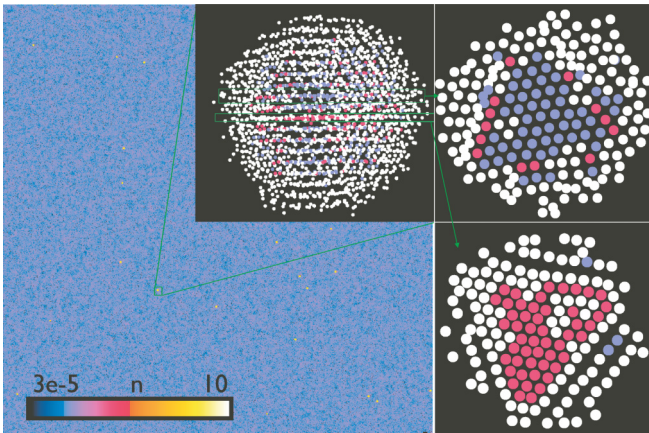


FIG. 3. A snapshot taken at the end of run T3n20L (after $1.16 \times 10^6 \tau$). The left panel shows a slice at a depth of 640σ of the entire box, $4272\sigma \times 4272\sigma$. The color map represents the local number density. A large cluster (2313 molecules) and two slices through the cluster are also shown, where blue is fcc, red is hcp, and white is unknown/amorphous.

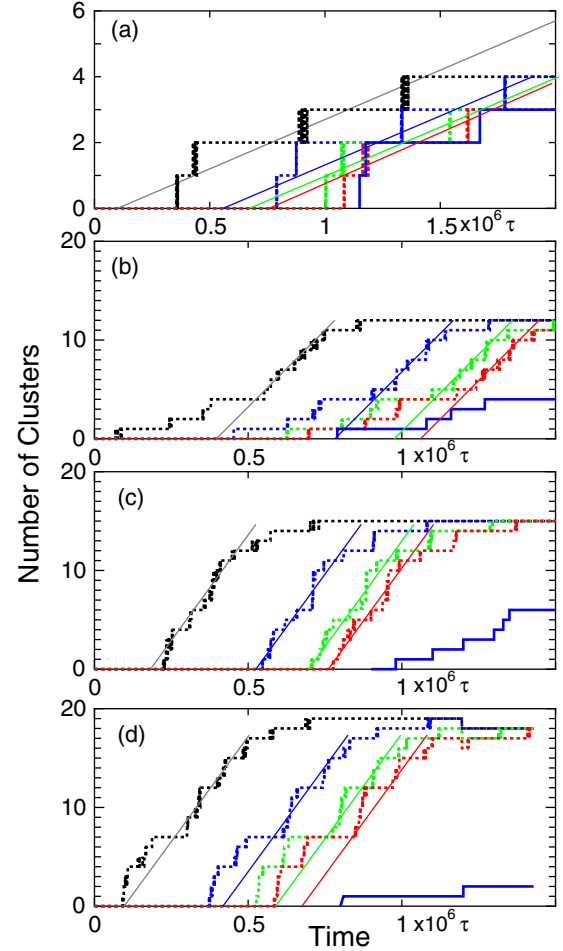


FIG. 4. The same as Fig. 1 but for runs T3n18 (a), T3n20S (b), T3n22 (c), and T3n24 (d). The slopes of thin lines show the obtained nucleation rates of the vapor-to-liquid transition at each run.

Figure 4 shows the same as Fig. 1, but for runs T3n18 (a), T3n20S (b), T3n22 (c), and T3n24 (d). The rate of nucleation of the vapor-to-liquid transition increased with the density of the monomer, $J = 2.8 \times 10^{-16} \sigma^{-3} \tau^{-1}$, $3.1 \times 10^{-15} \sigma^{-3} \tau^{-1}$, $4.9 \times 10^{-15} \sigma^{-3} \tau^{-1}$, and $5.3 \times 10^{-15} \sigma^{-3} \tau^{-1}$, respectively, which agreed well with our previous results for MD simulations and analytical evaluations [29,37]. The nucleation rate of the liquid-to-solid transition was $J_c = 7.2 \times 10^{-10} \sigma^{-3} \tau^{-1}$, $J_c = 4.9 \times 10^{-10} \sigma^{-3} \tau^{-1}$, $J_c = 7.0 \times 10^{-10} \sigma^{-3} \tau^{-1}$, and $J_c = 1.2 \times 10^{-10} \sigma^{-3} \tau^{-1}$, respectively.

In this study, we performed the simulations with the NVE ensemble because there is a possibility that the thermostat in the simulation can influence the crystallization of the particles. In the Appendix, we present the results of MD simulations with the NVT ensemble and compare them with the NVE simulations. The results imply that both vapor-to-liquid and liquid-to-solid nucleations occur earlier in the case of NVT than in NVE because of the higher temperatures in the NVE simulations (see the Appendix). The differences in the nucleation rates are not very large (up to several tens of percent for vapor-liquid nucleation, or a factor of 3 for liquid-to-solid nucleation).

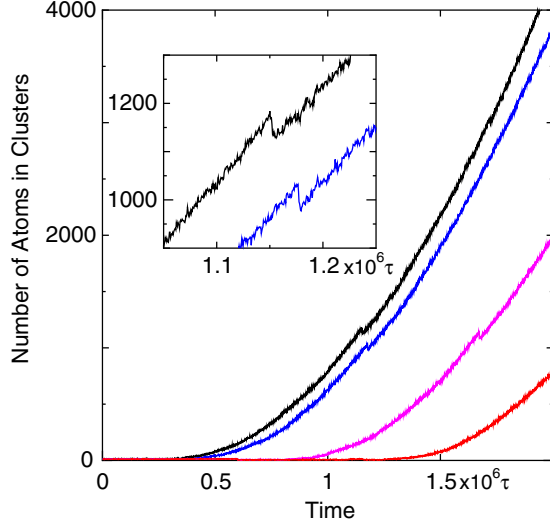


FIG. 5. Time evolution of the number of atoms for the four largest clusters in run T3n18. The three largest clusters suffered mass losses at crystallization. A closeup of the mass losses of the two largest clusters is also shown. They lost $\sim 5\%$ of their masses at $t = 1.15 \times 10^6 \tau$ and $1.17 \times 10^6 \tau$.

B. Evaporation at cluster crystallization

We found an interesting process associated with crystallization: evaporation at crystallization. Figure 5 shows the growth of the four clusters obtained in run T3n18. We observed crystallization of three clusters in this simulation. All of them suffered mass losses when they were crystallized. The magnitude of each instance of mass loss was a few percentage points of total mass (see Fig. 5).

Figure 6 shows the detailed evolution of the largest cluster at crystallization. The top panel shows the evolution of cluster mass, and the middle and bottom panels represent the number of atoms in the fcc or hcp structures recognized by the CNA method, and the temperature of the cluster, respectively. The number of atoms in the fcc and hcp structures began increasing at $t = 1.1517 \times 10^6 \tau$, and their rapid increase terminated at $t = 1.1520 \times 10^6 \tau$. This indicates that the crystallization of the cluster occurred quickly.

The latent heat due to the deposition of vapor atoms to the cluster heated up the cluster to $T \simeq 0.5\epsilon/k$ from a vapor temperature of 0.3. The gaseous temperature excluding the clusters remained low ($\simeq 0.3$) because we performed the simulations using the NVE ensembles. The latent heat due to crystallization further caused the cluster to become hotter than before crystallization. However, the temperature never reached the melting temperature of the bulk, which is 0.69 for LJ molecules [38,39]. This is due to cooling caused by evaporation from the cluster. The evaporation stabilizes the crystallized cluster. As seen at Fig. 6(a), the mass loss occurred immediately after crystallization and the heating up of the cluster at $t = 1.152 \times 10^6 \tau$.

C. Crystal growth

From the simulations, we obtained the growth rate of crystals in the clusters. Figure 7 shows a snapshot of a cluster

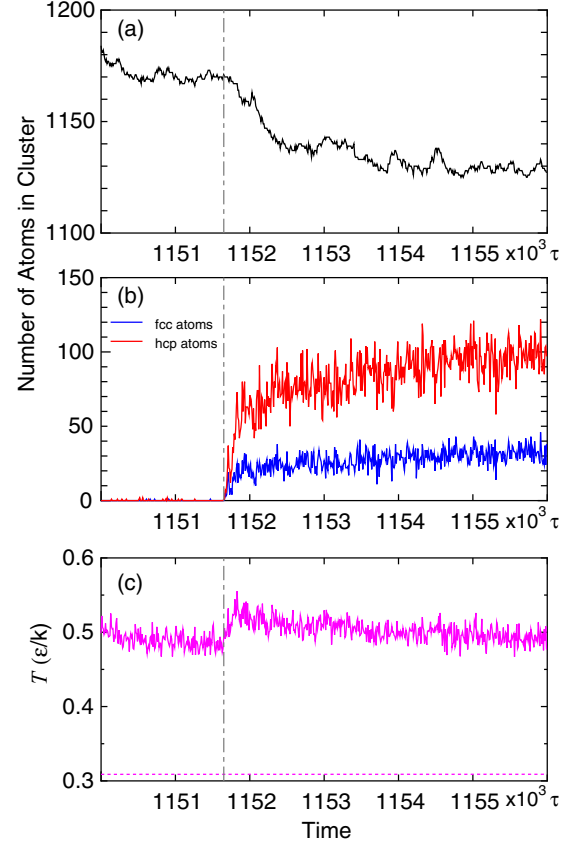


FIG. 6. (a) Time evolution of the number of atoms in the largest cluster in run T3n18. (b) The number of atoms in the fcc structure (blue) and the hcp structure (red) recognized by the CNA method in the largest cluster. (c) The average temperature of the largest cluster. The gaseous temperature excluding the cluster is represented using the dotted line. The dashed-dotted lines show the onset time of the crystallization.

composed of ~ 1000 molecules during the crystallization around $1.1769 \times 10^6 \tau$. The crystallization occurred very quickly. It started at $\sim 2\sigma$ from the center of the cluster [Fig. 7(a)]. The time interval of crystallization was only $\sim 100\tau$, as shown in Fig. 7. Figure 8 shows the growth rate of the crystal $di_c^{1/3}/dt$, where i_c is the total number of fcc and hcp atoms, including the crystal in the cluster. From the MD simulations, the growth rate was calculated to be approximately $0.04 \sigma/\tau$. The growth rate of the crystalline structure can be given by [40,41]

$$\frac{da}{dt} = Dn^{1/3} \left[1 - \exp\left(-\frac{\Delta h}{kT} \frac{T_m - T}{T_m}\right) \right], \quad (2)$$

where D is the self-diffusion coefficient, n is the number density of molecules in the liquid particle, T_m is the melting temperature, and Δh is the latent heat of crystallization per atom. The second term in the brackets in Eq. (2) indicates the effect of remelting the crystalline surface due to latent heat deposition. Comparing the growth rate obtained by the MD simulations, i.e., $di_c^{1/3}/dt = 0.04\sigma/\tau$, with Eq. (2), we obtain

$$D = 0.044 \quad (\sigma^2/\tau), \quad (3)$$

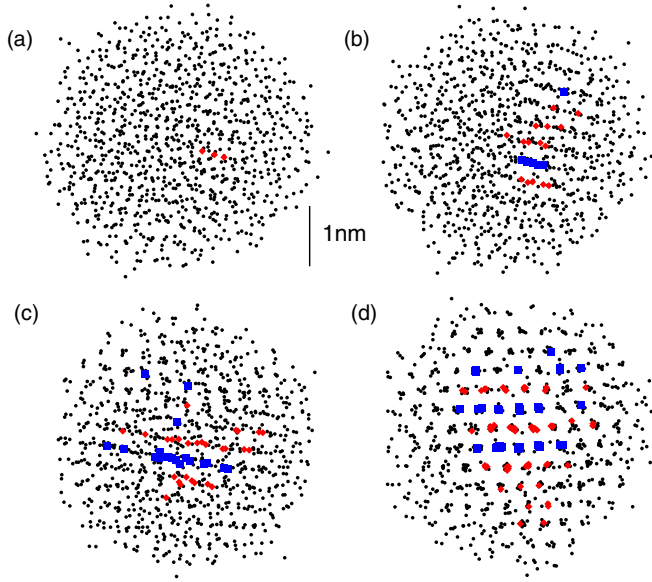


FIG. 7. Four snapshots for the second largest cluster during its crystallization at $t = 1.1769 \times 10^6 \tau + \Delta t$ in run T3n18, where $\Delta t = 0$ (a), 40τ (b), 60τ (c), and 100τ (d). The blue and red dots show atoms in fcc and hcp structures, respectively.

where we used $i = (4\pi/3)a^3n$, $\Delta h = 0.58\epsilon$ [42], $T \simeq 0.5\epsilon/k$, $T_m = 0.69\epsilon/k$ [38], and $n = 0.92\sigma^{-3}$ [29]. The diffusion coefficient of the liquid at $T \simeq 0.5\epsilon/k$ obtained in [44] was approximately 0.01, which is smaller than our calculated value. This indicates that molecules in small droplets were more diffusive than in the bulk liquid due to the surface effect of the finite boundary and lower density than the bulk liquid [32].

D. Comparison with the nucleation model for crystallization

We compared the liquid-to-solid nucleation rates obtained by our MD simulations with those of the nucleation theory of crystallization. The formula for the nucleation rate is given by [39,42,43]

$$J_c = nZf \exp\left\{-\frac{\Delta G^*}{kT}\right\}, \quad (4)$$

where Z is the Zeldovich factor, and f [τ^{-1}] is the attachment rate of molecules to a critical cluster of size i_* . Using the impinging rate of molecules per surface molecule $Dn^{2/3}$ with the self-diffusion coefficient D and the number of surface molecule of a critical cluster $Ai_*^{2/3}n^{2/3}$, f is given by

$$f = Ai_*^{2/3}n^{4/3}D. \quad (5)$$

ΔG^* in Eq. (4) is the minimum work needed to form an embryo of critical size i_* , and it is given by

$$\Delta G = -\Delta\mu i + \gamma Ai^{2/3}, \quad (6)$$

where γ is the interfacial tension between the liquid and the crystalline phases. $Ai^{2/3} (= 4\pi r_0^2 i^{2/3})$ is the surface area of an embryo of size i , and $\Delta\mu$ is the difference in chemical potential between the liquid and crystalline phases given by $\Delta\mu = \Delta h(T_m - T)/T_m$. Using critical size $i_* = 8(A\gamma)^3/(27\Delta\mu^3)$ and $Z = 1/(3i_*^{2/3})\sqrt{A\gamma/(\pi kT)}$, the nucleation rate can be

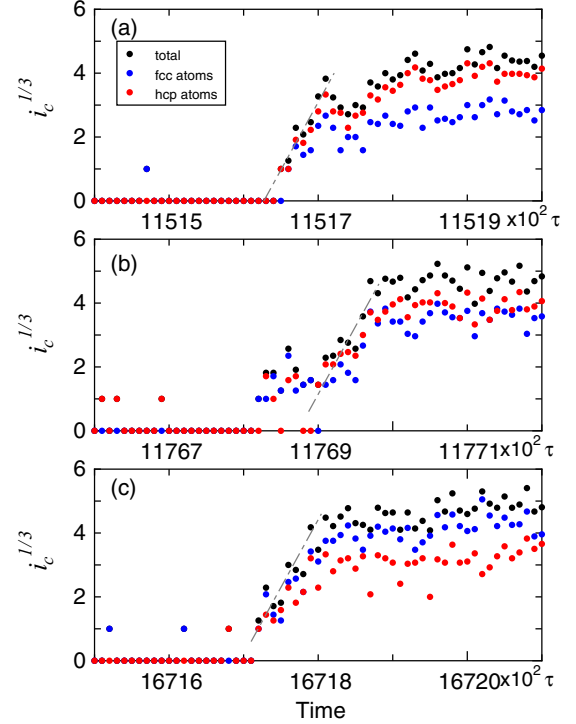


FIG. 8. The growth rate of the crystal in three clusters obtained in run T3n18. The dashed-dotted line shows $di_c^{1/3}/dt = 0.04\sigma/\tau$, where i_c is the number of atoms with fcc and fcp structures of crystal in the clusters (black dots). The blue and red dots correspond to fcc and hcp atoms, respectively.

rewritten as

$$J_c = \frac{A}{3}n^{7/3}\sqrt{\frac{A\gamma}{\pi kT}}D \times \exp\left[-\frac{4}{27}\frac{[A\gamma/(kT)]^3}{(\Delta h/kT)^2}\left(\frac{T_m}{T_m - T}\right)^2\right]. \quad (7)$$

Figure 9 shows the nucleation rate for crystallization as a function of interfacial tension. The solid lines represent the theoretical predictions of Eq. (7). The nucleation rate obtained from the MD simulations is shown by the dotted-dashed line. As shown in Fig. 9, our result suggests that interfacial tension corresponds to $0.23 \pm 0.005 \epsilon\sigma^{-2}$ at $T \simeq 0.5 \epsilon/k$. A few data items have been presented for flat solid-liquid interfacial tension of LJ molecules in the past work, where the potential cutoff radius was set to 2.5σ in simulations: $\gamma = 0.36, 0.54,$ and $0.8 \epsilon\sigma^{-2}$ at $T = 0.62, 1.0,$ and $1.5 \epsilon/k$ [45]. A study of crystal nucleation in bulk LJ liquid by [39] reported the values of $\gamma = (0.28-0.3)\epsilon\sigma^{-2}$ for $T \simeq 0.45\epsilon/k$.

In [42], the nucleation rates were obtained by MD simulations of 600 LJ molecules with a potential cutoff radius of 15σ , and γ was evaluated from the fitting of the obtained nucleation rates as $\gamma = 0.13\epsilon\sigma^{-2}$ at $T = (0.35-0.485)\epsilon/k$, which is smaller than that obtained in our calculation. The reasons for the difference between our calculation of γ and that of [42] may be considered. First is the temperature difference: in [42], the temperature was maintained with the Nosé-Hoover thermostat. As shown in the Appendix, crystallization occurs

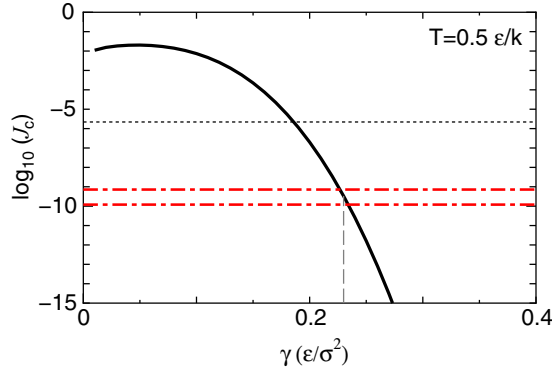


FIG. 9. Nucleation rate for crystallization as a function of the interfacial tension. The solid line is the theoretical prediction by classical nucleation theory at $T = 0.5\epsilon/k$. The maximum and minimum values of the nucleation rates by our MD simulations are shown by the dotted-dashed lines. Our results suggest that the interfacial tension between liquid and crystalline is $\gamma = 0.23 \pm 0.005\epsilon\sigma^{-2}$. The dotted line shows the results obtained in [42] at $T = 0.485\epsilon/k$.

earlier in the simulation with the NVT ensemble than with the NVE ensemble because of the higher temperatures in the NVE simulations. Consequently, the nucleation rate of crystallization is higher in NVT than in NVE , although the difference in the nucleation rates is not very large, as shown in the Appendix.

A more plausible reason is the different values of other parameters in the formula of the nucleation rate such as the melting temperature. In [42], T_m was set to $0.61 \epsilon/k$ corresponding to the melting temperature of LJ molecules with a potential cutoff radius of 2.5σ [39]. However, a higher melting temperature (e.g., $T_m = 0.69 \epsilon/k$ with a potential cutoff radius of 6.8σ) is preferable because T_m depends on the potential cutoff radius [39]. Using $T_m = 0.69 \epsilon/k$, the interfacial tension was calculated to be about $\gamma \simeq 0.2\epsilon\sigma^{-2}$, which was a similar value to our calculation (see Fig. 9). It is also possible that the interfacial tension depends not only on temperature, but also on such quantities as nucleus size.

E. Crystalline structures of clusters

The solid clusters composed of 1000–5000 molecules yielded typical structures in our simulations. Figure 10 shows the projections of the atomic positions in several solid clusters (4122–4422 atoms). The right panel in Fig. 10 also shows the positions of atoms recognized as having an fcc (or hcp) structure through analysis. Each had a characteristic structure for nanoparticles, i.e., icosahedral (Ih), decahedral (Dh), fcc-rich, and hcp-rich structures. As shown in Figs. 10(a) and 10(b), tenfold and fivefold symmetry axes were visible for the Ih and Dh structures. These structures were observed in nanoparticles for various substances [15,20]. In Fig. 10(a), the total number of fcc and hcp structures recognized by CNA in Ih was 808, where the number of fcc and hcp structures was, respectively, 336 and 472. These atoms were concentrated in the core of the cluster. In the cluster for Dh [Fig. 10(b)], the total number of fcc and hcp structures was larger than that of Ih, i.e., 1223 atoms for Dh, and the ratio of fcc to hcp was

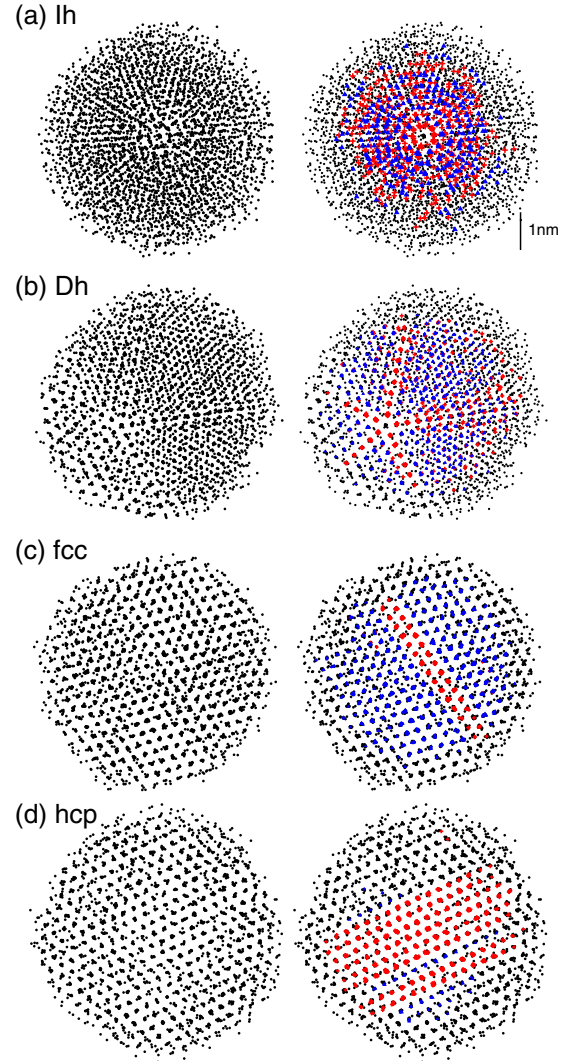


FIG. 10. Typical examples of clusters: (a) The atomic structure of the cluster is Ih. The cluster size is 4122, and the number of atoms with fcc and hcp recognized by CNA is 808 (fcc is 336, hcp is 472, and fcc/hcp is 0.711). (b) The atomic structure of cluster is Dh. The cluster size is 4160, and the number of atoms with fcc and hcp recognized by CNA is 1235 (fcc is 771, hcp is 464, and fcc/hcp is 1.66). (c) The fcc-rich structure. The cluster size is 4302. The number of atoms with fcc and hcp recognized by CNA is 1364 (fcc is 1119, hcp is 245, and fcc/hcp is 4.56). (d) The hcp-rich structure. The cluster size is 4185. The number of atoms with fcc and hcp recognized by CNA is 1090 (fcc is 78, hcp is 1012, and fcc/hcp is 0.077).

larger. In Fig. 10(c), we see an almost perfect crystal inside the cluster with some stacking faults. The ratio of fcc and hcp structures in the fcc-rich cluster was 4.6, significantly greater than those of Ih and Dh. In Fig. 10(d), we see similar structures to those in Fig. 10(c), but the number of hcp structures was greater than those in fcc. The temperatures of all clusters were high, $T \sim 0.51\epsilon/k$, due to the latent heat for crystallization. Figure 11(a) shows the structure factor of each cluster. These factors were similar among various structures. We found the first peak split in an fcc-rich structure. The results were in agreement with those of Ikeshoji *et al.* [15]. Figure 11(b) shows the potential energy per an atom E/i for both liquid and crystal

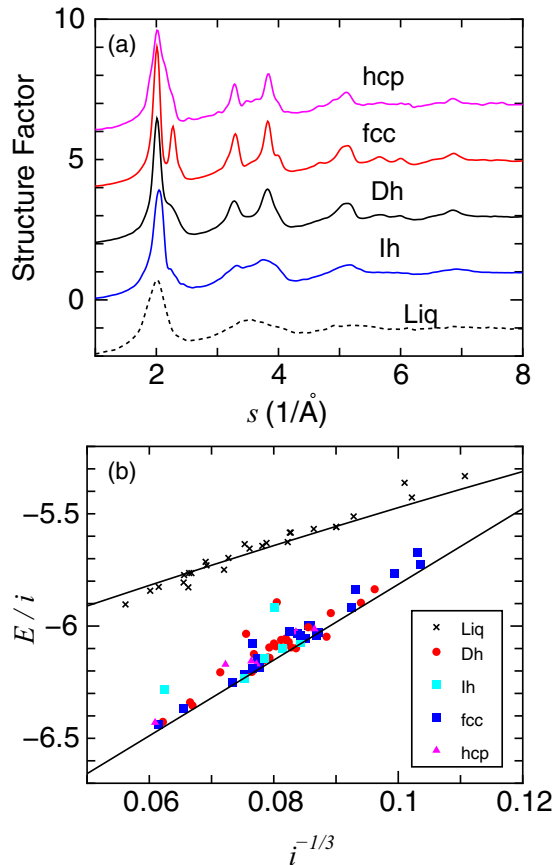


FIG. 11. (a) Structure factors of clusters of varying Ih, Dh, fcc-rich, and hcp-rich structures. (b) Potential energy per atom of supercooled liquid clusters and various crystalline clusters.

clusters, showing that the potential energy of the crystals was considerably smaller than that of the liquidlike particles, and there was no significant difference among crystals with different structures.

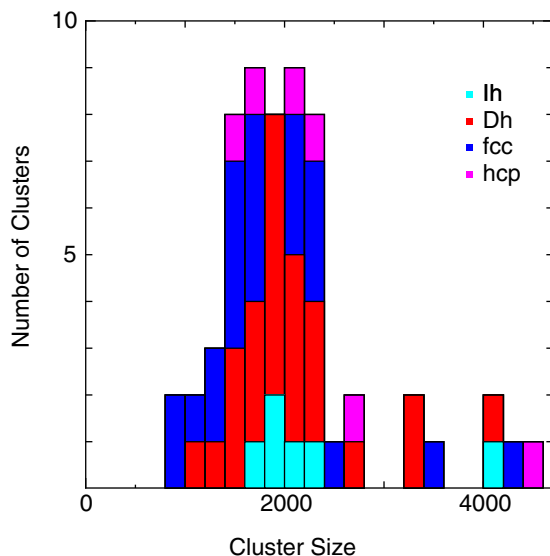


FIG. 12. Size distributions of the clusters of various structures: Ih (light blue), Dh (red), fcc-rich (blue), and hcp-rich (pink).

Figure 12 shows the size distribution of the crystalline particles with different structures obtained in our MD simulations. Our simulations showed that different structures of clusters coexisted in the same size range of 1000–5000 molecules. Each crystal retained its structure during growth, although the fcc structure was stable for rare gases [16]. In work by Doye and Calvo [16], the cluster structure with minimum energy was Ih for a size smaller than ~ 2000 molecules, whereas it was Dh for ~ 2000 –10 000 molecules. In general, there exists an energy barrier to a transition from solid to solid. Our results imply that transitions to a stable crystalline phase do not occur easily because of the energy barriers. Our results agreed with those of previous studies, suggesting that several kinds of clusters can coexist in the same size range, such that structural transitions are not sharp [19,20]. If the clusters grow further, the third step of nucleation occurs to form stable clusters, although we did not observe this in our simulations.

IV. SUMMARY AND CONCLUSION

In this paper, we reported molecular dynamical (MD) simulations of homogeneous vapor-to-solid nucleation. The results can be summarized as follows:

(i) The nuclei of liquid first appeared even at temperatures lower than the triple point. They crystallized after growing to a certain size (~ 800 at $T = 0.5\epsilon/k$). The smaller clusters did not crystallize.

(ii) All crystallized clusters lost 2–5 % of their masses at crystallization. The mass loss was caused by evaporation, since the latent heat due to crystallization heated up the cluster. The evaporation stabilizes the crystallized nanoclusters.

(iii) The solid clusters yielded four structures: icosahedral, decahedral, fcc-rich, and hcp-rich. Our results showed that clusters with different structures coexist in the same size range. The clusters maintained their structure during growth. This implies that the solid-solid transition does not easily occur due to the energy barriers to the transitions.

Our results suggest multiple steps from the transition from vapor to solid phase. In the first step of nucleation, the nuclei of liquid with a few tens of molecules form. The number and the size distribution of the particles are controlled by the first nucleation. In the second step of nucleation, metastable phases appear in many forms and grow. The additional nucleation process for solid-solid transitions is necessary to form a stable crystalline phase. Recent experimental studies [3–5] support multiple processes of nucleation for various substances. This is a common phenomenon in the first stage of condensation from vapor to solid.

ACKNOWLEDGMENTS

We are grateful to Y. Kimura and the anonymous reviewers for valuable comments. Numerical computations were carried out on the 3000 core cluster zBox4 at the Institute for Computational Science, Univ. of Zurich and on Cray XC30 at the Center for Computational Astrophysics, National Astronomical Observatory of Japan. This work was supported in part by JSPS KAKENHI Grants No. 15K05015, No. 15H05731, No. 16H00927, and No. 26287101.

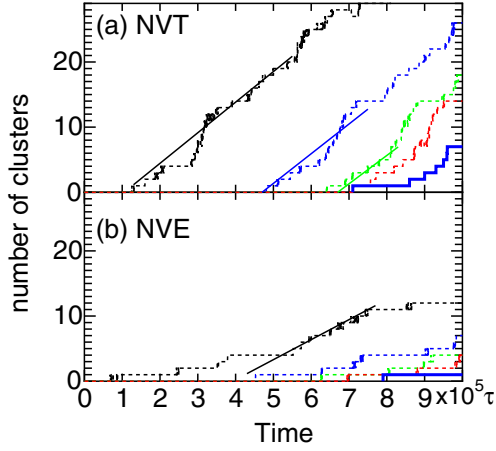


FIG. 13. The same as Fig. 1 but for T3n20S (a) and simulation in the NVT ensemble under the same initial conditions of T3n20S (b).

APPENDIX: COMPARISON BETWEEN NVT AND NVE

To investigate the effect of a thermostat in MD simulation on the crystallization of the particles, we performed MD simulations in an NVT ensemble with the same initial conditions of temperature and pressure for run T3n20S. The comparison is shown in Fig. 13. In the case of NVT , the rate of nucleation of the vapor-to-liquid transition is $4.0 \times 10^{-15} \sigma^{-3} \tau^{-1}$, which is larger than that of NVE by 40%. In addition, the nucleation rate of the liquid-to-solid transition is $J_c = 7.2 \times 10^{-10} \sigma^{-3} \tau^{-1}$, which is larger than that of NVE by a factor of 3.

The results imply that both vapor-to-liquid and liquid-to-solid nucleations occur earlier in the case of NVT than in NVE . The higher vapor-to-liquid nucleation rate in NVT is because of the difference in gaseous temperature since a slight temperature change can lead to a large difference in the nucleation rate. The ratio of nucleation rates J_1 and J_2 with different temperatures T_1 and T_2 and supersaturation ratios S_1 and S_2 is approximately evaluated from $J_1/J_2 \simeq (S_1/S_2)^{i_c-1}$, where i_c is the size of the critical cluster in the vapor-to-liquid nucleation. With this formula, we obtain $J_1 = 1.4J_2$ for $T_1 = 0.305 \varepsilon/k$ and $T_2 = 0.30 \varepsilon/k$, where we use $i_c (\simeq 11)$ and $S_1/S_2 = \exp[-H(1/T_1 - 1/T_2)]$, with $H = 6.9117$, which is the coefficient at saturation pressure for the Lennard-Jones molecule [29]. In our simulation, the temperature was $0.309 \varepsilon/k$ in the vapor-to-liquid nucleation phase in T3n20S, whereas it was $T = 0.3 \varepsilon/k$ in the NVT simulation. From the above estimation, the difference between the nucleation rates of NVE and NVT can be explained by the small difference in gaseous temperature.

The nucleation rate of the liquid-to-solid transition as well as the vapor-to-liquid transition in the case of NVT was larger than that in the case of NVE because of the temperature difference between the clusters of the NVT and NVE ensembles. The comparison of the cluster temperatures is shown in Fig. 14. Figure 14 shows the evolution of the largest cluster mass and the number of atoms in the fcc or hcp structures (a) and the cluster temperature (b). The dotted lines indicate the results of T3n20S, and the solid lines indicate the results of the simulation with the NVT ensemble, which was

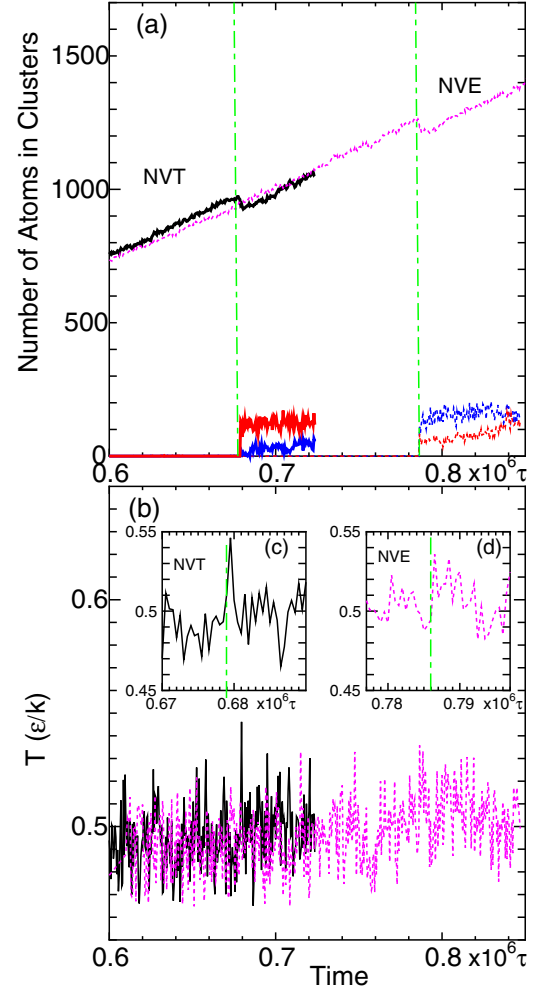


FIG. 14. Evolutions of the largest cluster mass and the number of atoms in fcc or hcp structures (a) and the cluster temperatures (b). The dotted lines indicate the results for T3n20S, and the solid lines indicate the results of the simulation with the NVT ensemble, where the simulation is performed from the time $4 \times 10^6 \tau$ with the result obtained by the run T3n20S. Parts (c) and (d) show the temperature evolutions around the crystallization time in the NVT and NVE ensembles, where dotted-dashed lines show the crystallization times.

performed from the time $4 \times 10^6 \tau$ with the result obtained by the run T3n20S.

As shown in Fig. 14(a), the crystallization time is $6.79 \times 10^5 \tau$ in the NVT simulation, while it is $7.86 \times 10^5 \tau$ in the NVE simulation; this implies that the cluster in the NVT simulation crystallized earlier than in the NVE simulation by about 10%. As shown in Fig. 14(b), the temperatures of the clusters in the NVT and NVE simulations are similar. However, the average temperature just before the crystallization in NVT is $0.485 \varepsilon/k$, which is lower than that of NVE ($0.503 \varepsilon/k$). Moreover, we found that after crystallization, the temperature decreased more rapidly in the NVT simulation than in the NVE simulation, as shown in Fig. 14(b). The temperature decrease in the NVT simulation is due to the thermostat because part of the latent heat released during crystallization is artificially removed from the interior of the clusters through it.

- [1] W. Ostwald, *Z. Phys. Chem.* **22**, 289 (1897).
- [2] T. Takahachi, *J. Cryst. Growth* **59**, 441 (1982).
- [3] Y. Kimura, K. K. Tanaka, H. Miura, and K. Tsukamoto, *Cryst. Growth Des.* **12**, 3278 (2012).
- [4] S. Ishizuka, Y. Kimura, and I. Sakon, *Astrophys. J.* **803**, 88 (2015).
- [5] S. Ishizuka, Y. Kimura, T. Yamazaki, T. Hama, N. Watanabe, and A. Kouchi, *Chem. Mater.* **28**, 8732 (2016).
- [6] P. R. ten Wolde, M. J. Ruiz-Montero, and D. Frenkel, *Phys. Rev. Lett.* **75**, 2714 (1995).
- [7] *Clusters and Nanomaterials: Theory and Experiment*, edited by Y. Kawazoe, T. Kondow, and K. Ohno (Springer, Berlin, 2002).
- [8] P. G. Vekilov, *Cryst. Growth Des.* **10**, 5007 (2010).
- [9] M. P. Pileni, *J. Phys.: Condens. Matter* **23**, 503102 (2011).
- [10] S. Ino, *J. Phys. Soc. Jpn.* **27**, 941 (1969).
- [11] J. Farges, M. F. de Feraudy, B. Raoult, and G. Torchet, *J. Chem. Phys.* **84**, 3491 (1986).
- [12] R. W. Hasse, *Phys. Lett. A* **161**, 130 (1991).
- [13] B. W. van de Waal, G. Torchet, and M.-F. de Feraudy, *Chem. Phys. Lett.* **331**, 57 (2000).
- [14] S. C. Hendy and B. D. Hall, *Phys. Rev. B* **64**, 085425 (2001).
- [15] T. Ikeshoji, G. Torchet, M. F. de Feraudy, and K. Koga, *Phys. Rev. E* **63**, 031101 (2001).
- [16] J. P. K. Doye and F. Calvo, *J. Chem. Phys.* **116**, 8307 (2002).
- [17] B. Hartke, *Angew. Chem., Inst. Ed.* **41**, 1468 (2002).
- [18] K. T. Koga and K. Sugawara, *Surf. Sci.* **529**, 23 (2003).
- [19] K. Koga, T. Ikeshoji, and K. I. Sugawara, *Phys. Rev. Lett.* **92**, 115507 (2004).
- [20] F. Baletto and R. Ferrando, *Rev. Mod. Phys.* **77**, 371 (2005).
- [21] W. Polak, *J. Cryst. Growth* **401**, 44 (2014).
- [22] M. Miki-Yoshida, L. Rendón, S. Tehuacanero, and M. José-Yacamán, *Surf. Sci.* **284**, L444, (1993).
- [23] K. Yasuoka and M. Matsumoto, *J. Chem. Phys.* **109**, 8451 (1998).
- [24] P. R. ten Wolde, M. J. R.- Montero, and D. Frenkel, *J. Chem. Phys.* **110**, 1592 (1999).
- [25] K. Laasonen, S. Wonczak, R. Strey, and A. Laaksonen, *J. Chem. Phys.* **113**, 9741 (2000).
- [26] S. Toxvaerd, *J. Chem. Phys.* **115**, 8913 (2001).
- [27] K. K. Tanaka, H. Tanaka, K. Kawamura, and K. Nakawasa, *J. Chem. Phys.* **122**, 184514 (2005).
- [28] J. Wedekind, J. Wölk, D. Regura, and R. Strey, *J. Chem. Phys.* **127**, 154515 (2007).
- [29] J. Diemand, R. Anglil, K. K. Tanaka, and H. Tanaka, *J. Chem. Phys.* **139**, 074309 (2013).
- [30] K. K. Tanaka, H. Tanaka, T. Yamamoto, and K. Kawamura, *J. Chem. Phys.* **134**, 204313 (2011).
- [31] S. Toxvaerd, *J. Chem. Phys.* **144**, 164502 (2016).
- [32] R. Angélil, J. Diemand, K. K. Tanaka, and H. Tanaka, *J. Chem. Phys.* **140**, 0744303 (2014).
- [33] J. Diemand, R. Angélil, K. K. Tanaka, and H. Tanaka, *Phys. Rev. E* **90**, 052407 (2014).
- [34] S. Plimpton, *J. Comput. Phys.* **117**, 1 (1995).
- [35] D. Faken and H. Jonsson, *Comp. Mater. Sci.* **2**, 279 (1994).
- [36] H. Tsuzuki, P. S. Branicio, and J. P. Rino, *Comput. Phys. Commun.* **177**, 518 (2007).
- [37] K. K. Tanaka, H. Tanaka, J. Diemand, and R. Angélil, *J. Chem. Phys.* **140**, 194310 (2014).
- [38] E. Mastny, and J. J. de Pablo, *J. Chem. Phys.* **127**, 104504 (2007).
- [39] V. G. Baidakov and A. O. Tipseev, *J. Chem. Phys.* **136**, 074510 (2012).
- [40] N. Okui, *J. Mater. Sci.* **25**, 1623 (1990).
- [41] A. Kouchi, T. Yamamoto, T. Kozasa, T. Kuroda, and J. M. Greenberg, *Astron. Astrophys.* **290**, 1009 (1994).
- [42] S. M. A. Malek, G. P. Morrow, and I. S-Voivod, *J. Chem. Phys.* **142**, 124506 (2015).
- [43] P. G. Debenedetti, *Metastable Liquids* (Princeton University Press, Princeton, NJ, 1996).
- [44] V. G. Baidakov, A. O. Tipseev, S. Bobrov, and G. V. Ionov, *J. Chem. Phys.* **132**, 234505 (2010).
- [45] R. L. Davidchack and B. B. Laird, *J. Chem. Phys.* **118**, 7651 (2003).